# Photocatalytic Removal of Polyester Polyurethane, and Polyethylene Microplastics via ZnO-Fe-Mg-C Nanocomposite to $H_2$

DELİA TERESA SPONZA, RUKİYE ÖZTEKİN*
Department of Environmental Engineering
Dokuz Eylül University
Tınaztepe Campus, 35160 Buca/Izmir,
TURKEY
* Corresponding Author

*Abstract:* - In this work $H_2$ generation was studied via polyester, polyurethane, and polyethylene microplastics using a novel nanocomposite namely zinc oxide-iron-magnesium-carbon (ZnO/Fe/Mg/C). The probability of $H_2$-production from plastic wastes was researched. The characterization of this nanocomposite were performed by XRD, FTIR, Raman, SEM, EDS and TEM analysis. XRD analysis showed that lattice planes of ZnO/Fe/Mg/C nanocomposite were distributed as (100), (002), (101), (102), (110), (103), (200), (112) and (004) according to FTIR analysis, it was found that the ligth abundances at 610, 682 and 779 $cm^{-1}$ were associated with the Zn and O moeities, while the maximum peak at 399 $cm^{-1}$ can be defined with Zn, Fe and Mg oxides and they connected to Zn and OH radicals. Raman spectra exhibited the G-band at 1499 $cm^{-1}$ as special properties of $sp^2$ carbonated moeities. SEM results showed that a brittle and porous structure containing spherical nanosized particles was detected in the ZnO/Fe/Mg/C nanocomposite, where various voids were formed, while the zinc particle size containing carbon-Mg-Fe was increased by excess carbon and ZnO/Fe/Mg/C nanocomposite. Furtheremore the effects of some operational conditions (time, nanocomposite concentration, temperature) on the yields of $H_2$ productions from both micropollutants were examined. The maximum $H_2$ production was detected at 250 mg/l polyethylene microplastic as 9800 ml/h with ZnO/Fe/Mg/C nanocomposite a, containing 2% Fe while the $H_2$ production was detected as 7800 ml/h from polyester polyurethane with the same nanocomposite. Optimum operating conditions; maximum $H_2$ production efficiencies of 99% polyethylene and 88% polyester polyurethane were achieved at 3 mg/l ZnO/Fe/Mg/C nanocomposite a, concentration, at 3 minutes and at 5 minutes experimental times and at 125°C temperature, respectively.

*Key-Words:* - Hydrogen ($H_2$) production; $H_2$, fuels; Microplastics; Polyester Polyethylene; Polyurethane; Photocatalytic removal; ZnO/Fe/Mg/C nanocomposite.

Received: November 17, 2023. Revised: April 21, 2024. Accepted: May 23, 2024. Published: June 20, 2024.

## 1 Introduction

In recent years microplastic wastes affect negatively the ecosystem. Microplastics are plastic wastes with a diameter < 5 mm. they cannot be treated from the ecosystems with some conventional processes since they have very small bodies, [1], [2]. Nanoplastics have a dimension of 0.1 μm. The remediation of microplastics is very important phenomenon since they have extensively used, [3], [4]. The novel progress is the recovery of microplastics to the economical valor having organics as ultimate end products. The polymers containing no olefins exhibited completely different structures from the plastics containing olefin. These products were: polyethylene (PE), polypropylene (PP), and polystyrene (PS), [5], [6], [7], [8], [9]. The physicochemical properties of microplastics based on fabrication procedure is effective in microplastic transformation. From remediation processes the polymers can be emitted to the ecosystems, [10]. Polystyrene, polyurethane and polyethylene was detected in municipal sludge and in environments containing garbage.

Polyethylene contained low weight carbon benzene and can be generated from the degradation of ethylene, [11], [12], [13], [14], [15], [16], [17], [18]. Polyethylene is a resin from polyolefin group. It is extensively utilized microplastic and can be generated from the food wrap and some plastic bottles and fuel boxes. It can degraded to fibers or and emitted from the rubbers. Types of polyethylene were summarized as follows, [19], [20], [21], [22], [23], [24]:

1. Low-Density Polyethylene (LDPE): LDPE is used extensively since it was not expensive. It can be suitable for plastic film applications like

grocery bags and food packaging. Despite its lower tensile strength and temperature resistance, LDPE's flexibility and toughness make it a popular choice in the market.

2. High-Density Polyethylene (HDPE): HDPE is praised for its high strength and stiffness. These attributes, combined with its resistance to many solvents, make it appropriate for extensive utilizations, from milk bottles to fuel tanks and piping systems.
3. Linear Low-Density Polyethylene (LLDPE): Bridging the gap between LDPE and HDPE, LLDPE offers superior tensile strength, large-scale deformability, and excellent resistance to environmental stress cracking. It is used in applications like stretch wrap, toys, and flexible tubing.

Nano sized ZnO, was extensively utilized in drinking and polluted water remediations, since has elevated redox potential, elevated electron activity and good photocatalytic activity, [12], [14]. ZnO nanocomposite exhibited elevated surface and high durability compared to other metal oxides. This, cause to an excellent photodegradation activity, [15]. In order to extend the photocatalytic yields of ZnO, nonmetals, and carbonated chemicals can be doped on ZnO surface to improve the activity of electrons in holes, [20]. By combining of a metal, the photodegradation yields can be elevated since redox reactions improve the light activity. These improves the surface resonance of the photocatalyst. Electromagnetic band gap energies of the metal nanocomposites resulting in transformation of electrons from valence band (VB) to conduction band (CB) ending with photocatalysis, [14], [19], [20], [21], [22], [23]. The presence of $Ni^{2+}$ and $Fe^{3+}$ in the nanocomposites cause to super magnetic structure of Ni ferrites, [11], [12], [14], [19], [20], [21], [22], [23]. Combining of ZnO with some metals like Fe, and Ni was performed to improve its ferro magnetic properties, [15], [24], [25]. The recent studies showed that photodegradation properties were performed by ZnO connected with certain ratios of $NiFe_2O_4$, [26], [27]. The Photoactivity of nano composites are influenced by the generation rules, nanocomposite diameter, and certain ratios of dopant molecules. Fe-Ni nanocomposites were utilized are used to photodegrade the microplastic residues with excessive $H_2$ productions.

The doping of Fe to Ni improved the nanocomposite activity, [28], [29], [30], [31], [32]. Physicochemical analysis results indicated that doping of Ni increase the metal nanocomposite diameter and oxygen releasing. Fe-Ni nanocomposite show high catalytic performance resulting in 98% hydrogen production from microplastic residues. Ni having nanocomposites exhibited excellent performance due to C and H bond degradation ending with excellent photocatalytic performances, [20], [22]. Nano metal oxides having Zn, Mg and Ca exhibits excellent microbial inhibitions, [33], [34], [35], [36], [37], [38]. In recent works, it was found that, ZnO nanocomposites exhibited inhibitions versus microorganisms, [39], [40], [41], [42], [43], [44], [45], [46], [47]. The recent literature showed that antimicrobial effects of ZnO NPs. In some studies, emissions of $Zn^{2+}$ from nanocomposites cause to death of microorganisms, [48], [49], [50]. It is important to note that the solubility of ZnO is very low.

Carbon nanotubes (CNT) were used for remediate the pollutants. CNT structure and its electro equations can be changed quickly by doping of some metals to its surface, [21]. CNT was effectively used since is elastic and has some mechanical, and electrical structures ending with hydrogen production, drug transportation and treatment of polluted ecosystems. CNT can be utilized to energy storage with high electrolyte properties, and equilibrium. CNT exhibits excessive surface, fast reaction kinetic and degradation of pollutants like $Pb^{2+}$, $Cu^{2+}$, $Cd^{2+}$, and, dyes, [19], [23]. CNT have also been utilized for treatment of pollutants with perfect structure, conductive, and chemical structures, [11], [16], [24]. CNTs have a mesoporous structure and provides effective adsorption, [9], [15], [25].

In this study, the photodegradation of ZnO was improved by connecting Fe, Mg and C nanoparticles on the its structure, and the photodegradation capacity of ZnO/Fe/Mg/C nanocomposite was examined to produce $H_2$ from polyester polyurethane and polyethylene microplastics. The effect of time, temperature and nanocomposite concentrations on $H_2$ yields were studied for polyester polyurethane, and polyethylene microplastics.

# 2 Materials and Methods

## 2.1 Production of ZnO/Fe/Mg/C Nanocomposite

ZnO particles were produced from $Zn(NO_3)_2.6H_2O$ and NaOH was added to adjust the pH. 5.990 g of $Zn(NO_3)_2.6H_2O$ was mixed with 100 ml distilled water. The temperature was elevated and at a temperature of 70ºC, 1 ml of 4 M NaOH was added up to the mixture pH was become 10.0. After 2 h mixing a precipitate was found. This section was separated by a centrifuge. The filtered precipitate was dried at 90ºC for 10 h. The temperature was adjusted

to 500ºC for 2 h in an incubator. Then 10 g $ZnO(NO_3)_2.4H_2O$ was mixed in 200 ml of water. 1 ml of 6 M NaOH (6 M) was added to reach a pH of 9.0. To produce the $ZnO/Fe^{2+}$ (30%) nanocomposite, 0.600 g ZnO was added. 0.420 g $Fe(NO_3)_3.9H_2O$ was dissolved mixed in 20 ml water. The produced mixture was added to an autoclave at 190ºC for 28 h. The settled mass was dried.

MgO was produced by addition of $Mg(NO_3)_2.6H_2O$ as $Mg^{2+}$ addition, and settled by using NaOH, [29]. For MgO production, 0.32 M $Mg(NO_3)_2$ was added to 150 ml of distilled. Afterwards, 1 ml 2M NaOH solution was added to $Mg(NO_3)_2$ to reach a pH of 9.0. The settling of $Mg(OH)_2$ was performed. The produced precipitate was centrifuged and dried in an incubator at 140ºC for 6 h. Then, the powder was calcined at 700ºC for 7 h in an oven. The produced nanocomposite was ZnO/Fe/Mg/C nanocomposite.

### 2.2 Detection of Polyethylene and Polyester Polyurethane in GC-MS

600 mg of liquids were autoclaved at 141ºC for 30 min. The samples were centrifuged at 8000 rpm for 10 min at 4ºC. Then the liquids were maintained at −25ºC while the suspension was withdrawn. The pH was adjusted to 2.0 after 2 h. Then extracted with the passage of $N_2$ gas to a volume of 70 µl. The liquids were extracted with *N*,*O*-bis(trimethylsilyl)trifluoro acetamide before measurements in an Agilent 6890 model gas chromatography (GC) coupled with an Agilent model 5973 mass spectrometer (MS), in an GC-MS. The samples were separated on HP-5ms capillary column (40 m x 0.30 mm diameter x 0.35 µm film). The temperature was adjusted as follows: the initial temperature of 90ºC for 5 min and then at a temperature of 10ºC up to 230ºC.

### 2.3 Measurement of the Photodegradation Yield of the ZnO/Fe/Mg/C Nanocomposite

Photocatalytic degradation of catalysts was performed in 250 mg/l liquids. About 5 mg of ZnO/Fe/Mg/C nanocomposite was dissolved in 70 ml of deionized water. The microplastic photodegradations were performed in an GC-MS as aforementioned.

## 3 Results and Discussions

### 3.1 XRD Analysis Results of ZnO/Fe/Mg/C Nanocomposite

The first two and third specimen diffraction line profiles are determined from 2θ = 2º to 2θ = 100º. The created lattice planes of ZnO/Fe/Mg/C nanocomposite samples are indicated as (100), (002), (101), (102), (110), (103), (200), (112) and (004) (Fig. 1). These 2θ values were measured as 31.62º, 34.38º, 36.11º, 56.32º, 62.61º, 65.06º, 68.06º and 72.52º, respectively (Fig. 1). These planes are consistent with the standard spectra of the hexagonal phase of wurtzite-type ZnO with space group P63mc, defined by interpretation of the resulting PDF number 5-664. The diffraction peaks of the ZnO/Fe/Mg/C nanocomposite sample are of medium height and appear to be single peaks originating from the sample. Moreover, it is stated in the studies in the literature that no other peak from other crystalline phases provides the crystallinity conformation of ZnO, [26], [27], [51], [52], [53], [54].

* Fig. 1 can be found in the Appendix section.

XRD patterns of Fe-doped samples containing 2% and 4% Fe, ZnO/Fe/Mg/C nanocomposite a and ZnO/Fe/Mg/C nanocomposite b, showed corresponding diffraction peaks for another phase with ZnO crystallites without any peaks. Additionally, biomimetic production of ZnO using egg white and doping of various concentrations of iron oxide ($Fe_2O_3$) appeared to cause changes in all diffraction peaks and the height of both. 2% $Fe_2O_3$ doping brought about a decrease in the peak height in crystallites. The opposite behaviour was noticed in the case of the sample treated with 4 mol% $Fe_2O_3$. 2 mol% $Fe_2O_3$ Surface-doped ZnO/C system led to a gradual decrease in the crystallite size of ZnO, followed by an increase in strain and dislocation density. In the case of doping using 5 mol% $Fe_2O_3$, the opposite effect was observed. In general, doping the studied system with 2 or 5 mol% $Fe_2O_3$ caused a shift of one atom to its neighbour and an increase in the lattice constants.

### 3.2 FTIR Analysis Results of ZnO/Fe/Mg/C Nanocomposite

Fig. 2 shows the FTIR spectra of the components present in the nanocomposite. The metal-oxygen release mode corresponds to the absorption bands within 850 and 390 $cm^{-1}$ as shown in the FTIR spectrum.

* Fig. 2 can be found in the Appendix section.

The weak bands at 610, 682 and 779 $cm^{-1}$ related to the Zn–OH group, whereas the characteristic broad band at 399 $cm^{-1}$ is attributed to metal–oxide stretching vibrations of the Zn-O bond, [26], [27]. Vibrational modes of carbon groupings, together

with Mg and Fe, may be responsible for the bands at 1090 and 1480 $cm^{-1}$. Due to the capping agent in egg white, these bands are attributed to C–H, C–O and C–OH vibrations with the aforementioned metals, [26], [27], [28]. The strong bands at 1640 and 5000 $cm^{-1}$ are due to the stretching vibrations of O–H bonds with C, indicating the presence of the aforementioned metal during the preparation of the nanocomposite pellet, [29], [51]. As can be observed from the FTIR spectra, the addition of iron ions during doping caused a modest repositioning of every absorption band and a subsequent alteration in their intensities.

### 3.3 Raman Analysis Results of ZnO/Fe/Mg/C Nanocomposite

With Raman spectra, the vibrational properties of three separate samples materials are investigated. Fig. 3 displays the Raman spectra of the examined materials between 0 and 5000 $cm^{-1}$ at room temperature. The Raman spectra of the ZnO/Fe/Mg/C nanocomposite a, and ZnO/Fe/Mg/C nanocomposite b samples did not reveal the distinctive vibrational modes connected to ZnO crystals. However, these spectra show two large peaks in the G and D bands at 1499 $cm^{-1}$ and 2199 $cm^{-1}$, respectively.

* Fig. 3 can be found in the Appendix section.

Typical carbon compounds exhibiting these bands showed distinctive features, [55]. Indeed, the appearance of the G-band at 1499 $cm^{-1}$ is a significant characteristic of $sp^2$ hybridized carbon materials. This band can provide specific points in the in-plane vibration of $sp^2$ bonded carbon regions, [56]. On the other hand, the D-band occurs at 2199 $cm^{-1}$ indicates the existence of $sp^3$ defects or abnormalities inside the hexagonal graphitic structure, [33]. Additionally, the edges of this band may violate the symmetry and selection criteria, and may consist of amorphous carbon and hexagonal graphite structure, or a combination of these, [35], [53]. The crystallite shape of Fe with nanocomposites exhibiting Mg and Fe and is proportional to the relationship ($I_D/I_G$) corresponding to the intensities of these bands, confirming the formation of crystallized carbon.

It has been stated that increasing the dopant content in ZnO/Fe/Mg/C nanocomposite b causes an increase in the formation of amorphous carbon due to the severe weakness in the intensities of the G and D bands, [23], [26], [27], [57]. This finding indicates that the standard error of the carbon material decreases.

### 3.4 SEM Analysis Results of ZnO/Fe/Mg/C Nanocomposite

The SEM analysis is conducted to study the morphology of the biosynthesized pure and Fe-Mg doped ZnO/C nanoparticles (Fig. 4).

* Fig. 4 can be found in the Appendix section.

SEM images showed that the shape and size of the display fragile and porous flakes containing spherical nanosized particles with the formation of various voids in ZnO/Fe/Mg/C nanocomposite a, (Fig. 4a). In other words, the as-synthesized materials are easily broken or destroyed and also are easily crumbled. The carbon-Mg-Fe containing zinc particle size reduced via excess carbon and Fe in the ZnO/Fe/Mg/C nanocomposite b since it was a capping agent in the nanoparticles (Fig. 4b).

### 3.5 EDS Analysis Results of ZnO/Fe/Mg/C Nanocomposite

Table 1 describes the less fragmentation structure of the nanocomposite. As the surface area of the nanocomposite decreased, while the percentage of ZnO decreased to 3%. Under these conditions a slight decrease in the pores and voids sizes was detected due to the agglomeration of smaller nanoparticles, especially, in the ZnO/Fe/Mg/C nanocomposite b. This nanocomposite contains high amounts of Fe additives. This is demonstrated by the presence of the lowest surface area in the above-mentioned nanocomposite, [23], [26], [27], [57].

* Table 1 can be found in the Appendix section.

The EDS pattern of ZnO/Fe/Mg/C nanocomposite a, elementally, respectively; It shows the presence of Zn (28.39 wt%), O (13.60 wt%), C (26.74 wt%), Fe (12.67 wt%) and Mg (11.67 wt%) (Table 2).

* Table 2 can be found in the Appendix section.

The EDS patterns of ZnO/Fe/Mg/C nanocomposite b showed the elemental content of these samples, respectively: Zn (25.00wt%), Fe (20.01 wt% and 5.36 wt%), Mg (8.99 wt%), O (4.32 wt%) and C (10.06 wt%). All of these nanocomposites; It consists of the elements Zn, Fe, O, C and Mg.

### 3.6 TEM Analysis Results of ZnO/Fe/Mg/C Nanocomposite

The results of the TEM analysis confirm that both nanocomposite samples were encapsulated in graphitic carbon layers (Fig. 5).

* Fig. 5 can be found in the Appendix section.

In the ZnO/Fe/Mg/C nanocomposite an exhibited better dispersion, depending on a decrease in the agglomeration formation rate of the nanocomposite (Fig. 5a). While the average diameter of ZnO/Fe/Mg/C nanocomposite a was measured as 8.3 nm (Fig. 5a), ZnO/Fe/Mg/C nanocomposite b exhibited an increase in the agglomeration process, with a size diameter of 5.9 nm (Fig. 5b).

### 3.7 The Selected Area Electron Diffraction (SAED) Patterns of ZnO/Fe/Mg/C Nanocomposite

In Fig. 6a, Fig. 6b, and Fig. 6c, various bright spots were observed within the concentric rings, indicating the polycrystalline structure of pure and Fe-doped ZnO/C/Mg nanoparticles.

* Fig. 6 can be found in the Appendix section.

The Fe-doped ZnO/C/Mg nanoparticles b, demonstrated maximum intensity of these bright spots diminishes. In addition, increasing the Fe dopant content exhibited an increase in the number of concentric rings. These originated from the Fe-doped ZnO/C/Mg nanoparticles b size reduction, with the self-aggregation of some bulk layers, [58], [59], [60], [61].

### 3.8 $H_2$ Productions from 250 mg/l Polyester Polyurethane, and 250 mg/l Polyethylene via 3 mg/l ZnO/Fe/Mg/C Nanocomposite after 10 min Irradiation under 60 W/m$^2$ UV

The hydrolysis reaction of polyester polyurethane and polyethylene to $H_2$ was carried out within a 36-hour reaction time using Fe-doped samples containing 2% ZnO/Fe/Mg/C nanocomposite a and 4% ZnO/Fe/Mg/C nanocomposite b. The $H_2$ productions were 7800 ml/h and 5600 ml/h, respectively for polyester polyurethane while the $H_2$ productions were measured as 9800 ml/h and 8700 ml/h for polyethylene reduction at 125$^o$C (Table 3).

* Table 3 can be found in the Appendix section.

The $H_2$ productions were extremely high since polyethylene carbon bonds were lower than that of polyester polyurethane, [59], [60], [61]. ZnO/Fe/Mg/C nanocomposite a, with a Fe content of 2%, exhibited higher $H_2$ production than the other. Microplastic yields at low temperatures were 100% at 130$^o$C and 54% yield at 110$^o$C (Table 3).

The hydrolysis ratio of the polyethylene was found to be higher since was readily degraded to $H_2$. However, polyester polyurethane showed ineffective depolymerisations and small amounts of polyurethane oligomers were observed. High hydrolysis rate of water-soluble polyethylene ending with high $H_2$ productions. When polyester polyurethane conversion is not completed; A metabolite residue was recovered, indicating that polyester polyurethane polymers consist of a metabolite with a lower molecular weight. After use, the ZnO/Fe/Mg/C nanocomposite catalyst can be easily recovered by centrifugation, and reused in other catalytic experiments under the same conditions; this shows a slight decrease in $H_2$ production of 3% (data not shown), [47], [60], [61], [62], [63].

### 3.9 Effect of Nanocomposite Concentration on $H_2$ Productions in 250 mg/l Polyester Polyurethane and Polyethylene Microplastics after 10 min Irradiation under 60 W/m$^2$ UV

The effects of increasing ZnO/Fe/Mg/C nanocomposite a, catalyst concentration from 1, 3, 5, 7 and to 10 mg/l was detected on $H_2$ productions in both microplastics (Table 4).

* Table 4 can be found in the Appendix section.

The maximum degradation capacity of 250 mg/l polyester polyurethane was 89% while the degradation yield was 99% at 250 mg/l polyethylene concentration at 3 mg/l ZnO/Fe/Mg/C nanocomposite a with a Fe ratio of 2% (Table 4). Then, the degradation yields of both microplastics dropped slightly from 99% to 94% and from 89% to 80% at 7.0 mg/l nanocomposite concentrations, for polyethylene and polyester polyurethane microplastics. This may be because, at low nanocomposite dosages, nanocomposite sites are more exposed to microplastics and degradation has occurred more rapidly. On the other hand, there is additional numbers of unoccupied nanocomposite sites at higher nanocomposite concentrations, which reduces the photodegradation capacity.

### 3.10 Effect of Time on $H_2$ Productions in 250 mg/l Polyester Polyurethane and Polyethylene Microplastics via 3 mg/l ZnO/Fe/Mg/C Nanocomposite a

The effects of contacting time (3–30 min) on the photocatalytic degradation of both microplastics to $H_2$ were studied. The results showed that the degradation efficiencies of polyester polyurethane and polyethylene microplastics increase readily with increasing irradiation time interval from 3 min up to 6 mins. At the beginning the microplastic concentration is more for degradation which later decreased with time (Table 5).

* Table 5 can be found in the Appendix section.

This also may be because initially large number of metal radicals present in the solution and they were attacked on microplastic molecules with the time. When the metal radicals lowered, the speed of degradation process may also decrease. The percentage of degradation efficiency for polyester polyurethane and polyethylene microplastics were 88% and 99% after 4 min and 6 min, respectively. The degradation efficiency increased sharply at the beginning while the degradation rate of increases very rapidly up to 10 min in polyester polyurethane, and then the degradation rate decreases slightly after the optimum time. The maximum degradation time of polyethylene was detected after 4 min photodegradation then the yields decreased after 5 min.

### 3.11 Effect of Temperature on $H_2$ Production from Polyester Polyurethane and Polyethylene Microplastics via 3 mg/l ZnO/Fe/Mg/C Nanocomposite a

The effect of temperature on the thermal degradation rates of polymers has been extensively explored because of the need to predict the service lifetime of consumer plastics. In some studies, it was found that the results are consistent with an Arrhenius relationship, [14], [20], but other studies have found non-Arrhenius behavior, [21], [22], [23]. There is some indication that the non-Arrhenius behavior is due to the complex degradation pathways referred to above, and therefore the relatively straightforward degradation process in polymers with metal–metal bonds might provide some fundamental insights that are not obtainable with standard carbon-chain polymers.

The temperature dependence of the quantum yields for the degradation of polymer could depend on: (1) the inherent temperature dependence of the photolysis and radical trapping reaction of the ZnO/Fe/Mg/C nanocomposite a, (2) the temperature dependent behaviour of the polymer morphology, or (3) a temperature-dependent dynamical property of the photogenerated radicals in the polymer. There is a significant increase in the quantum yields for polyester polyurethane with increasing temperature. In contrast, for polyethylene dispersed with Mg–Fe-ZnO chromophores are unattached to the polymer chains there are only slight increases the quantum yields over this temperature range, [23], [26], [27], [47], [57], [58], [59], [60], [61], [62], [63]. Big increase in the quantum yield with temperature for polyester polyurethane is not attributable to an inherent temperature dependence of the photolysis and subsequent radical trapping reaction of the nanocomposite (Table 6).

* Table 6 can be found in the Appendix section.

Since the quantum yields for polyethylene dispersed show only a slight temperature dependence, the temperature dependence observed for polyester polyurethane. The maximum $H_2$ production rates were detected at a temperature of 125ºC with $H_2$ yields of 99% and 88% for polyethylene and polyester polyurethane microplastics, respectively. Like higher temperatures like 150ºC and 175ºC did not improve the $H_2$ yields.

## 4 Conclusions

$H_2$ production was examined by producing ZnO/Fe/Mg/C, a new nanocomposite from polyester polyurethane and polyethylene microplastics. The potential for converting plastic wastes to $H_2$ was studied in this study as fuel. Physicochemical analyses were performed to determine ZnO/Fe/Mg/C nanocomposite a, and ZnO/Fe/Mg/C nanocomposite b containing 2% and 4% Fe ratios.

Raman analyses showed that the G band at 1499 $cm^{-1}$ is an important feature of $sp^2$ hybridized carbon materials. The D-band occurs at 2199 $cm^{-1}$, and indicates the presence of $sp^3$ defects or abnormalities within the hexagonal graphite structure. The crystallite shape of Fe with nanocomposites exhibiting Mg, ZnO and C, and is proportional to the relationship ($I_D/I_G$) corresponding to the intensities of these bands, confirming the formation of crystallized carbon.

The selected area electron diffraction (SAED) results of the ZnO/Fe/Mg/C nanocomposite exhibited bright spots inside concentric rings, indicating the polycrystalline nature of the Fe-doped ZnO/C/Mg nanocomposites a. The 4% Fe-doped ZnO/C/Mg nanocomposites b, demonstrated maximum intensity of these bright spots. Elevated high Fe dopant content

exhibited an increase in the number of concentric rings resulting in size reduction.

Selected area electron diffraction (SAED) results of ZnO/Fe/Mg/C nanocomposite a exhibited bright spots within concentric rings; This case is based on Fe-doped ZnO/C/Mg nanocomposite a; It shows polycrystalline nature. ZnO/C/Mg nanocomposite b, containing 4% Fe exhibited an increase in the number of concentric rings, leading to size reduction.

The XRD analysis showed that lattice planes of ZnO/Mg/C/Fe nanocomposite were distributed as (100), (002), (101), (102), (110), (103), (200), (112) and (004).

According to FTIR analysis, the weak bands at 610, 682 and 779 $cm^{-1}$ are related to the Zn-OH group, while the characteristic broad band at 399 $cm^{-1}$ is; It was observed that metal-Zn-O with Mg and C bonds had oxide stretching vibrations.

Additionally, the effects of some operating conditions (time, nanocomposite concentration, temperature) on $H_2$ production from both micropollutants were investigated. The maximum $H_2$ production was detected at 250 mg/l polyethylene microplastic as 9800 ml/h with ZnO/Fe/Mg/C nanocomposite a, containing 2% Fe while the $H_2$ production was detected as 7800 ml/h from polyester polyurethane with the same nanocomposite.

Optimum operating conditions; maximum $H_2$ production efficiencies of 99% polyethylene and 88% polyester polyurethane were achieved at 3 mg/l ZnO/Fe/Mg/C nanocomposite a, concentration, at 3 min and at 5 min experimental times and at 125ºC temperature, respectively.

*Acknowledgement:*
Experimental analyzes in this study were performed at the Laboratories of the Canada Research Center, Ottawa, Canada. The authors would like to thank this body for providing financial support.

*References:*

[1] J. Chen, J. Wu, P.C. Sherrell, J. Chen, H. Wang, W.-X. Zhang, J. Yang, How to build a microplastics-free environment: strategies for microplastics degradation and plastics recycling, *Advanced Science*, Vol.9, No.6, 2022, 2103764.

[2] S. Chu, B. Zhang, X. Zhao, H.S. Soo, F. Wang, R. Xiao, H. Zhang, Photocatalytic conversion of plastic waste: from photodegradation to photosynthesis, *Advanced Energy Materials*, Vol.12, No.22, 2022, 2200435.

[3] W. Hamd, E.A. Daher, T.S. Tofa, J. Dutta, Recent advances in photocatalytic removal of microplastics: mechanisms, kinetic degradation, and reactor design, *Frontiers in Marine Science*, Vol.9, 2022, 885614.

[4] A. Xie, M. Jin, J. Zhu, Q. Zhou, L. Fu, W. Wu, Photocatalytic technologies for transformation and degradation of microplastics in the environment: current achievements and future prospects, *Catalysts*, Vol.13, 2023, 846, pp. 1-19.

[5] A.-U.-R. Bacha, I. Nabi, L. Zhang, Mechanisms and the engineering approaches for the degradation of microplastics, *ACS Environmental Science & Technology Engineering*, Vol.1, No.11, 2021, pp. 1481–1501.

[6] C.I. Pizarro-Ortega, D.C. Dioses-Salinas, M.D. Fernández Severini, A.D. Forero López, G.N. Rimondino, N.U. Benson, S. Dobaradaran, G.E. De-la-Torre, Degradation of plastics associated with the COVID-19 pandemic, *Marine Pollution Bulletin*, Vol.176, 2022, 113474.

[7] R. Kumar, Metal oxides-based nano/microstructures for photodegradation of microplastics, *Advanced Sustainable Systems*, Vol.7, No.6, 2023, 2300033.

[8] W. Li, W. Zhao, H. Zhu, Z.-J. Li, W. Wang, State of the art in the photochemical degradation of (micro)plastics: from fundamental principles to catalysts and applications, *Journal of Materials Chemistry A*, Vol.11, No.6, 2023, pp. 2503–2527.

[9] Y. Pan, S.-H. Gao, C. Ge, Q. Gao, S. Huang, Y. Kang, G. Luo, Z. Zhang, L. Fan, Y. Zhu, A.-J. Wang, Removing microplastics from aquatic environments: a critical review, *Environmental Science & Ecotechnology*, Vol.13, 2023, 100222.

[10] B. Sarkar, P.D. Dissanayake, N.S. Bolan, J.Y. Dar, M. Kumar, M.N. Haque, R. Mukhopadhyay, S. Ramanayaka, J.K. Biswas, D.C.W. Tsang, J. Rinklebe, Y.S. Ok, Challenges and opportunities in sustainable management of microplastics and nanoplastics in the environment, *Environmental Research*, Vol.207, 2022, 112179.

[11] L. Wang, A. Kaeppler, D. Fischer, J. Simmchen, Photocatalytic $TiO_2$ micromotors for removal of microplastics and suspended matter, *ACS Applied Materials & Interfaces*, Vol.11, No.36, 2019, pp. 32937–32944.

[12] B.E. Llorente-García, J.M. Hernández-López, A.A. Zaldívar-Cadena, C. Siligardi, E.I. Cedillo-González, First insights into photocatalytic

degradation of HDPE and LDPE microplastics by a mesoporous N–$TiO_2$ coating: effect of size and shape of microplastics, *Coatings*, Vol.10, No.7, 2020, 658.

[13] S.M. Beladi-Mousavi, S. Hermanová, Y. Ying, J. Plutnar, M. Pumera, A maze in plastic wastes: autonomous motile photocatalytic microrobots against microplastics, *ACS Applied Materials & Interfaces*, Vol.13, No.21, 2021, pp. 25102–25110.

[14] C. Venkataramana, S.M. Botsa, P. Shyamala, R. Muralikrishna, Photocatalytic degradation of polyethylene plastics by $NiAl_2O_4$ spinels-synthesis and characterization, *Chemosphere*, Vol.265, 2021, 129021.

[15] X. Feng, R. Long, C. Liu, X. Liu, Visible-light-driven removal of tetracycline hydrochloride and microplastics (HDPE) by nano flower hybrid heterojunction $NH_2$-MIL-88B(Fe)/$MoS_2$ via enhanced electron-transfer, *Separation and Purification Technology*, Vol.302, 2022, 122138.

[16] M. Urso, M. Pumera, Nano/microplastics capture and degradation by autonomous nano/microrobots: a perspective, *Advanced Functional Materials*, Vol.32, No.20, 2022, 2112120.

[17] N.O. Dos Santos, R. Busquets, L.C. Campos, Insights into the removal of microplastics and microfibers by advanced oxidation processes, *Science of the Total Environment*, Vol.861, 2023, 160665.

[18] J. He, L. Han, F. Wang, C. Ma, Y. Cai, W. Ma, E.G. Xu, B. Xing, Z. Yang, Photocatalytic strategy to mitigate microplastic pollution in aquatic environments: promising catalysts, efficiencies, mechanisms, and ecological risks, *Critical Reviews in Environmental Science and Technology*, Vol.53, No.4, 2023, pp. 504–526.

[19] M.C. Ariza-Tarazona, J.F. Villarreal-Chiu, J.M. Hernández-López, J. Rivera De la Rosa, V. Barbieri, C. Siligardi, E.I. Cedillo-González, Microplastic pollution reduction by a carbon and nitrogen-doped $TiO_2$: effect of pH and temperature in the photocatalytic degradation process, *Journal of Hazardous Materials*, Vol.395, 2020, 122632.

[20] X. Jiao, K. Zheng, Q. Chen, X. Li, Y. Li, W. Shao, J. Xu, J. Zhu, Y. Pan, Y. Sun, Y. Xie, Photocatalytic conversion of waste plastics into $C_2$ fuels under simulated natural environment conditions, *Angewandte Chemie International Edition*, Vol.59, No.36, 2020, pp. 15497–15501.

[21] J.-M. Lee, R. Busquets, I.-C. Choi, S.-H. Lee, J.-K. Kim, L.C. Campos, Photocatalytic degradation of polyamide 66; evaluating the feasibility of photocatalysis as a microfibre-targeting technology, *Water*, Vol.12, No.12, 2020, 3551.

[22] I. Nabi, A.U. Bacha, K. Li, H. Cheng, T. Wang, Y. Liu, S. Ajmal, Y. Yang, Y. Feng, L. Zhang, Complete photocatalytic mineralization of microplastic on $TiO_2$ nanoparticle film, *iScience*, Vol.23, No.7, 2020, 101326.

[23] A.D. Vital-Grappin, M.C. Ariza-Tarazona, V.M. Luna-Hernández, J.F. Villarreal-Chiu, J.M. Hernández-López, C. Siligardi, E.I. Cedillo-González, The role of the reactive species involved in the photocatalytic degradation of HDPE microplastics using C,N-$TiO_2$ powders, *Polymers*, Vol.13, No.7, 2021, 999.

[24] L. Ding, X. Guo, S. Du, F. Cui, Y. Zhang, P. Liu, Z. Ouyang, H. Jia, L. Zhu, Insight into the photodegradation of microplastics boosted by iron (Hydr)oxides, *Environmental Science & Technology*, Vol.56, No.24, 2022, pp. 17785–17794.

[25] R. Jiang, G. Lu, Z. Yan, J. Liu, D. Wu, Y. Wang, Microplastic degradation by hydroxy-rich bismuth oxychloride, *Journal of Hazardous Materials*, Vol.405, 2021, 124247.

[26] T.S. Tofa, K.L. Kunjali, S. Paul, J. Dutta, Visible light photocatalytic degradation of microplastic residues with zinc oxide nanorods, *Environmental Chemistry Letters*, Vol.17, No.3, 2019a, pp. 1341–1346.

[27] T.S. Tofa, F. Ye, K.L. Kunjali, J. Dutta, Enhanced visible light photodegradation of microplastic fragments with plasmonic platinum/zinc oxide nanorod photocatalysts, Catalysts, Vol.9, No.10, 2019b, 819.

[28] A.A. Adesina, Industrial exploitation of photocatalysis: progress, perspectives and prospects, *Catalysis Surveys from Asia*, Vol.8, No.4, 2004, pp. 265–273.

[29] M. Aguilar-Vega, *Structure and Mechanical Properties of Polymers*, in Handbook of Polymer Synthesis, Characterization, and Processing, E. Saldívar-Guerra, E. Vivaldo-Lima (Editors), John Wiley & Sons, Inc., Hoboken, NJ, United States, 2013, pp. 425–434.

[30] D.O. Adekoya, M. Tahir, N.A.S. Amin, G-$C_3N_4$/(Cu/$TiO_2$) Nanocomposite for enhanced photoreduction of $CO_2$ to $CH_3OH$ and HCOOH under UV/visible light, *Journal of $CO_2$ Utilization Part C*, Vol.18, 2017, pp. 261-274.

[31] S. Abbasi, A. Sarafraz-Yazdi, A. Amiri, F. Ghaemi, Development of novel magnetic solid-phase extraction sorbent based on $Fe_3O_4$/carbon

nanosphere/polypyrrole composite and their application to the enrichment of polycyclic aromatic hydrocarbons from water samples prior to GC–FID analysis, *Journal of the Iranian Chemical Society*, Vol.15, No.1, 2018, pp. 153–161.

[32] A. Uheida, H.G. Mejía, M. Abdel-Rehim, W. Hamd, J. Dutta, Visible light photocatalytic degradation of polypropylene microplastics in a continuous water flow system, *Journal of Hazardous Materials*, Vol.406, 2021, 124299.

[33] O.M. Alfano, D. Bahnemann, A.E. Cassano, R. Dillert, R. Goslich, Photocatalysis in water environments using artificial and solar light, *Catalysis Today*, Vol.58, No.2-3, 2000, pp. 199–230.

[34] M.E. Ali, M.N. Rahman, S.M. Sarkar, S.B.A. Hamid, Heterogeneous metal catalysts for oxidation reactions, *Journal of Nanomaterials*, Vol.2014, 2014, Article ID 192038.

[35] S.S. Ali, I.A. Qazi, M. Arshad, Z. Khan, T.C. Voice, C. Mehmood, Photocatalytic degradation of low-density polyethylene (LDPE) films using titania nanotubes, *Environmental Nanotechnology, Monitoring and Management*, Vol.5, 2016, pp. 44–53.

[36] O. Alvarado-Rolon, R. Natividad, R. Romero, L. Hurtado, A. Ramírez-Serrano, Modelling and simulation of the radiant field in an annular heterogeneous photoreactor using a four-flux model, *International Journal of Photoenergy*, 2018, 1678385, pp. 1–16.

[37] J. Almond, P. Sugumaar, M.N. Wenzel, G. Hill, C. Wallis, Determination of the carbonyl index of polyethylene and polypropylene using specified area under band methodology with ATR-FTIR spectroscopy, *e-Polymers*. Vol.20, No.1, 2020, pp. 369–381.

[38] P.H. Allé, P. Garcia-Muñoz, K. Adouby, N. Keller, D. Robert, Efficient photocatalytic mineralization of polymethylmethacrylate and polystyrene nanoplastics by $TiO_2$/β-SiC alveolar foams, *Environmental Chemistry Letters*, Vol.19, No.2, 2021, pp. 1803–1808.

[39] A. Barlow, R.S. Lehrle, J.C. Robb, Direct examination of polymer degradation by gas chromatography: I. applications to polymer analysis and characterization, *Polymer*, Vol.2, 1961, pp. 27–40.

[40] J.D. Andrade, *Surface and Interfacial Aspects of Biomedical Polymers*: Volume 1 Surface Chemistry and Physics, Springer, Boston, MA, United States), 1985.

[41] A.M. Amat, A. Arques, M.A. Miranda, S. Seguí, Photo-fenton reaction for the abatement of commercial surfactants in a solar pilot plant, *Solar Energy*, Vol.77, No.5, 2004, pp. 559–566.

[42] A.M. Amat, A. Arques, F. López, M.A. Miranda, Solar photo-catalysis to remove paper mill wastewater pollutants, *Solar Energy*, Vol.79, No.4, 2005, pp. 393–401.

[43] V. Augugliaro, M. Litter, L. Palmisano, J. Soria, The combination of heterogeneous photocatalysis with chemical and physical operations: a tool for improving the photo process performance, *Journal of Photochemistry and Photobiology C: Photochemistry Reviews*, Vol.7, No.4, 2006, pp. 127–144.

[44] E.R. Bandala, C. Estrada, Comparison of solar collection geometries for application to photocatalytic degradation of organic contaminants, *Journal of Solar Energy Engineering*, Vol.129, No.1, 2007, pp. 22–26.

[45] M.A. Browne, T.S. Galloway, R.C. Thompson, Spatial patterns of plastic debris along estuarine shorelines, *Environmental Science & Technology*, Vol.44, No.9, 2010, pp. 3404–3409.

[46] M. Bagheri, M. Mohseni, A study of enhanced performance of VUV/UV process for the degradation of micropollutants from contaminated water, *Journal of Hazardous Materials*, Vol.294, 2015, pp. 1–8.

[47] M.C. Ariza-Tarazona, J.F. Villarreal-Chiu, V. Barbieri, C. Siligardi, E.I. Cedillo-González, New strategy for microplastic degradation: green photocatalysis using a protein-based porous N-$TiO_2$ semiconductor, *Ceramics International Part B*, Vol.45, No.7, 2019, pp. 9618–9624.

[48] A.E. Cassano, C.A. Martin, R.J. Brandi, O.M. Alfano, Photoreactor analysis and design: fundamentals and applications, *Industrial & Engineering Chemistry Research*, Vol.34, No.7, 1995, pp. 2155–2201.

[49] A.E. Cassano, O.M. Alfano, Reaction engineering of suspended solid heterogeneous photocatalytic reactors, *Catalysis Today*, Vol.58, No.2-3, 2000, pp. 167–197.

[50] Y. Cao, M. Zhao, X. Ma, Y. Song, S. Zuo, H. Li, W. Deng, Critical review on the interactions of microplastics with heavy metals: mechanism and their combined effect on organisms and humans, *Science of the Total Environment*, Vol.788, 2021, 147620.

[51] M. Eriksen, L.C.M. Lebreton, H.S. Carson, M. Thiel, C.J. Moore, J.C. Borerro, F. Galgani, P.G. Ryan, J. Reisser, Plastic pollution in the world's oceans: more than 5 trillion plastic pieces

weighing over 250,000 tons afloat at sea, *PLoS One*, Vol.9, No.12, 2014, e111913.
[52] X. Cui, W. Li, P. Ryabchuk, K. Junge, M. Beller, Bridging homogeneous and heterogeneous catalysis by heterogeneous single-metal-site catalysts, *Nature Catalysis*, Vol.1, No.6, 2018, pp. 385–397.
[53] F. Miao, Y. Liu, M. Gao, X. Yu, P. Xiao, M. Wang, S. Wang, X. Wang, Degradation of polyvinyl chloride microplastics via an electro-Fenton-like system with a $TiO_2$/graphite cathode, Journal of Hazardous Materials, 399, 2020, 123023.
[54] L.P. Domínguez-Jaimes, E.I. Cedillo-González, E. Luévano-Hipólito, J.D. Acuña-Bedoya, J.M. Hernández-López, Degradation of primary nano-plastics by photocatalysis using different anodized $TiO_2$ structures, *Journal of Hazardous Materials*, Vol.413, 2021, 125452.
[55] B. Ahmed, E. Limem, A. Abdel-Wahab, B. Nasr, Photo-Fenton treatment of actual agro-industrial wastewaters, *Industrial & Engineering Chemistry Research*, Vol.50, No.11, 2011, pp. 6673–6680.
[56] B. Alfaifi, H. Ullah, S. Alfaifi, A. Tahir, T. Mallick, Photoelectrochemical solar water splitting: from basic principles to advanced devices, *Veruscript Functional Nanomaterials*, Vol.2, No.12, 2018, BDJOC3.
[57] A. Uheida, H.G. Mejía, M. Abdel-Rehim, W. Hamd, J. Dutta, Visible light photocatalytic degradation of polypropylene microplastics in a continuous water flow system, Journal of Hazardous Materials, Vol.406, 2021, 124299.
[58] H. Luo, Y. Xiang, T. Tian, X. Pan, An AFM-IR study on surface properties of nano-$TiO_2$ coated polyethylene (PE) thin film as influenced by photocatalytic aging process, *Science of the Total Environment*, Vol.757, 2021, 143900.
[59] J. Ge, Z. Zhang, Z. Ouyang, M. Shang, P. Liu, H. Li, X. Guo, Photocatalytic degradation of (micro)plastics using $TiO_2$-based and other catalysts: properties, influencing factor, and mechanism, *Environmental Research*, Vol.209, 2022, 112729.
[60] M.C. Rex, A. Mukherjee, Prospects of $TiO_2$-based photocatalytic degradation of microplastic leachates related disposable facemask, a major COVID-19 waste, *Frontiers in Nanotechnology.*, Vol.4, 2022, pp. 1-15.
[61] M. Saifuddin, Y. Ghaffari, S.Y. Park, C.G. Kim, Rapid surface degradation of co-axially arranged polypropylene globules by nanoporous carbonized $TiO_2$ assisted with UV-C, *Environmental Research*, Vol.212, 2022, 113422.
[62] R. Verma, S. Singh, M.K. Dalai, M. Saravanan, V.V. Agrawal, A.K. Srivastava, Photocatalytic degradation of polypropylene film using $TiO_2$-based nanomaterials under solar irradiation, *Materials and Design*, Vol.133, 2017, pp. 10–18.
[63] S.Y. Tan, W.C. Chong, S. Sethupathi, Y.L. Pang, L.C. Sim, E. Mahmoudi, Optimisation of aqueous phase low density polyethylene degradation by graphene oxide-zinc oxide photocatalysts, *Chemical Engineering Research and Design*, Vol.190, 2023, pp. 550–565.

## Contribution of Individual Authors to the Creation of a Scientific Article (Ghostwriting Policy)

Prof. Dr. Delia Teresa Sponza and Post-Dr. Rukiye Öztekin took an active role in every stage of the preparation of this article.
The authors equally contributed in the present research, at all stages from the formulation of the problem to the final findings and solution.

## Sources of Funding for Research Presented in a Scientific Article or Scientific Article Itself

This research study was undertaken in the Environmental Microbiology Laboratories at Dokuz Eylül University Engineering Faculty Environmental Engineering Department, İzmir, Turkey. The authors would like to thank this body for providing financial support.

## Conflict of Interest

The authors have no conflicts of interest to declare that are relevant to the content of this article.

## APPENDIX

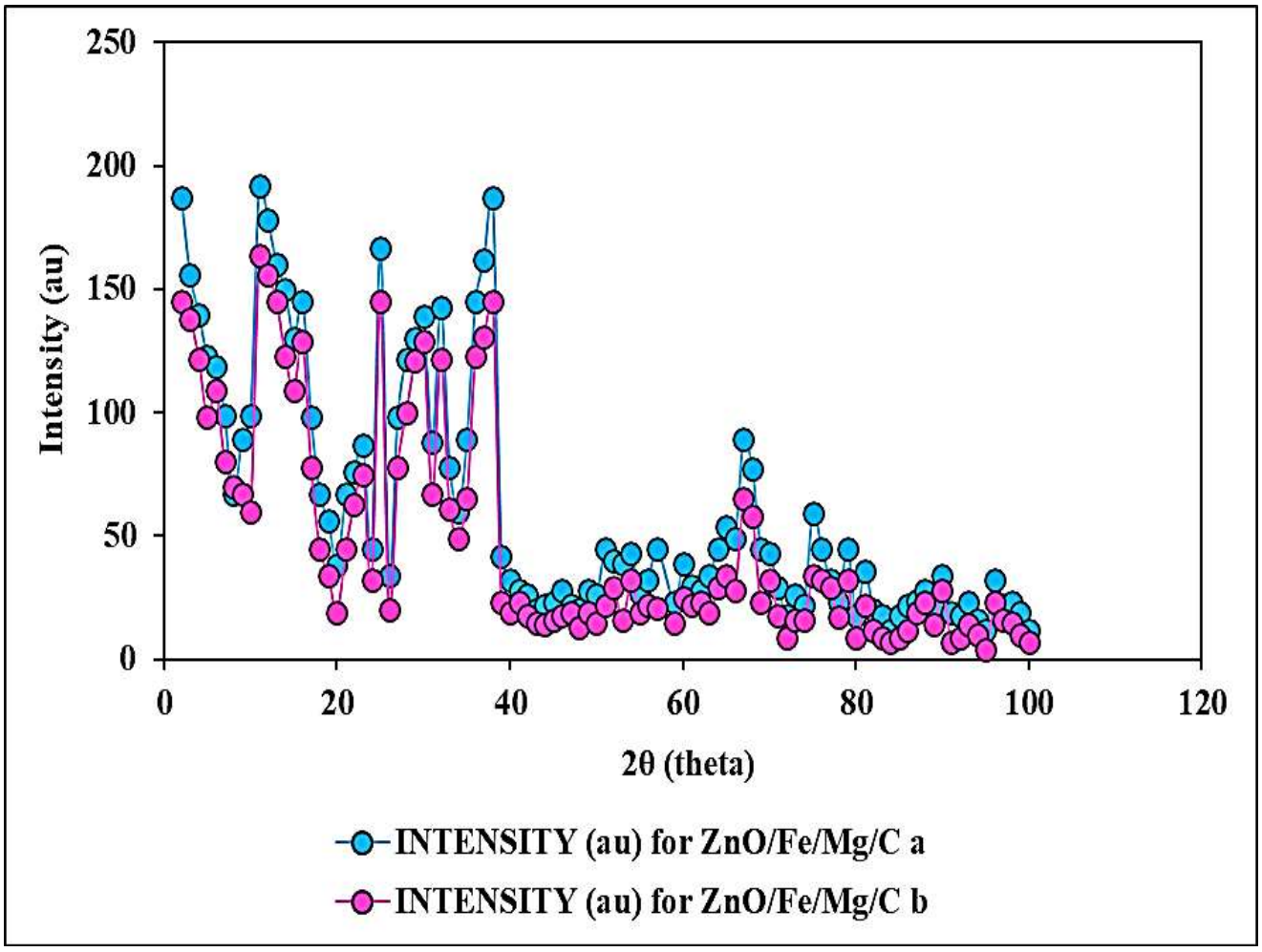


**Fig. 1.** XRD spectra of ZnO/Fe/Mg/C nanocomposite

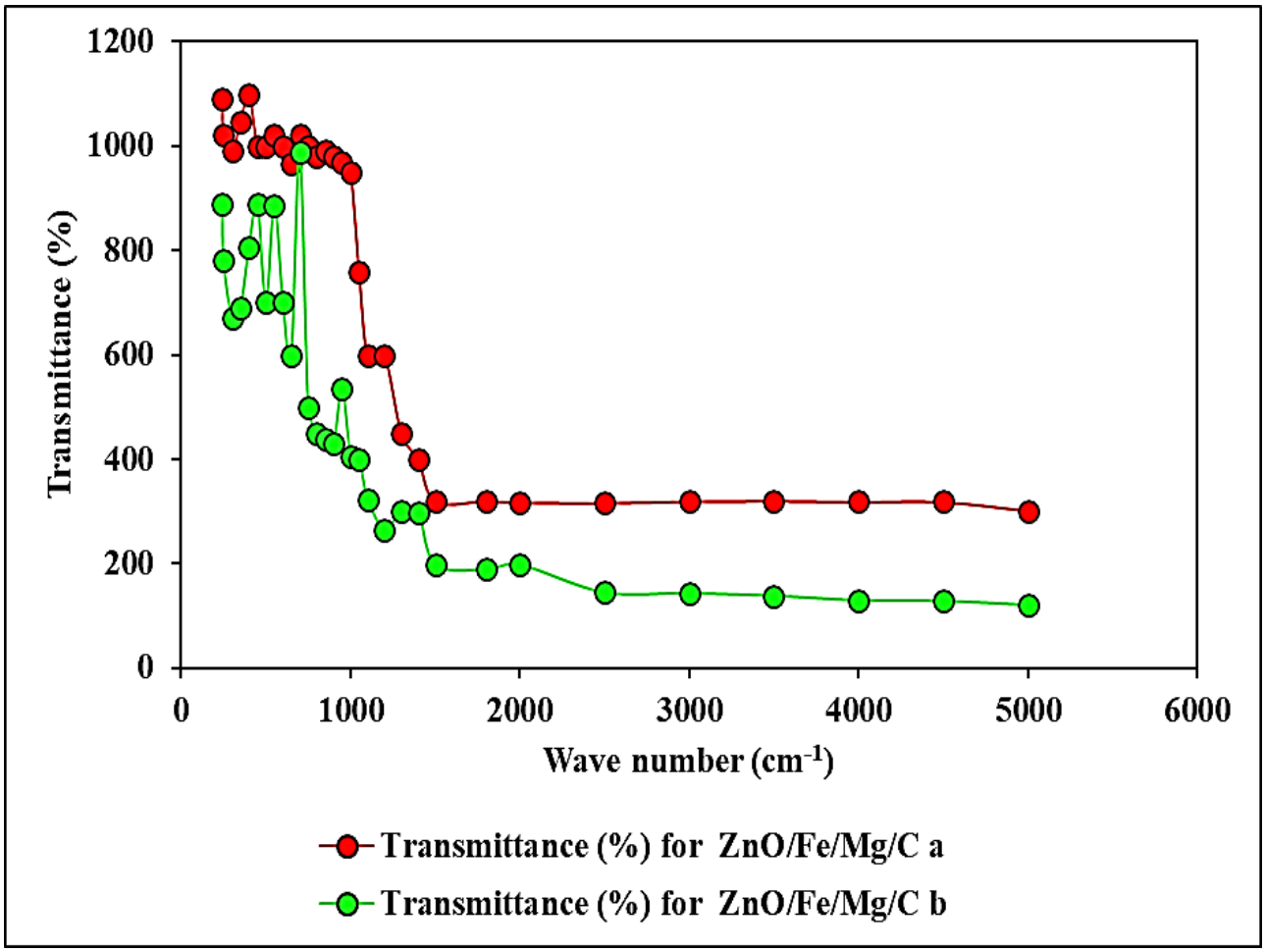


**Fig. 2.** FTIR spectra of ZnO/Fe/Mg/C nanocomposite

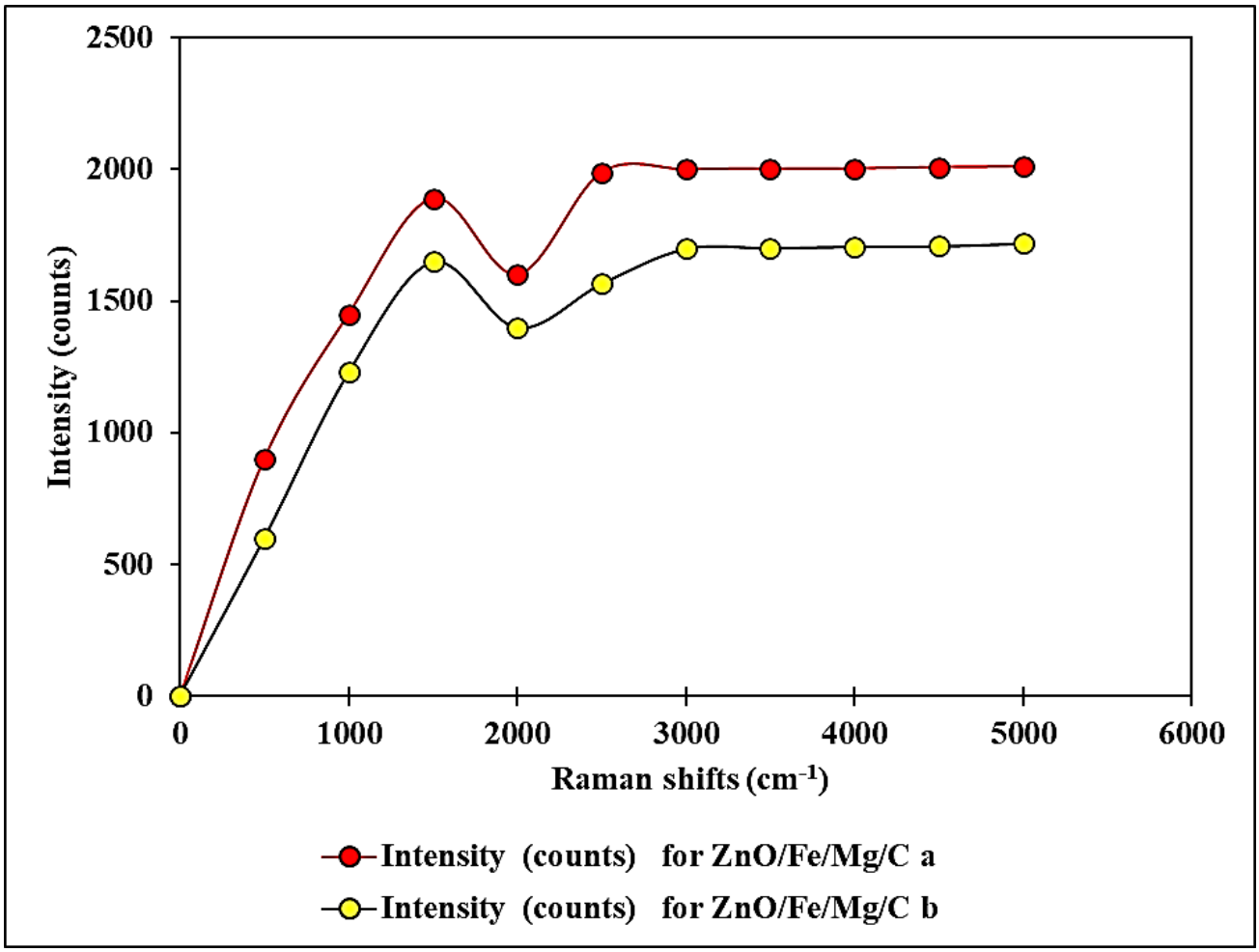


**Fig. 3.** Vibrational Raman spectra of ZnO/Fe/Mg/C nanocomposite

**(a)**

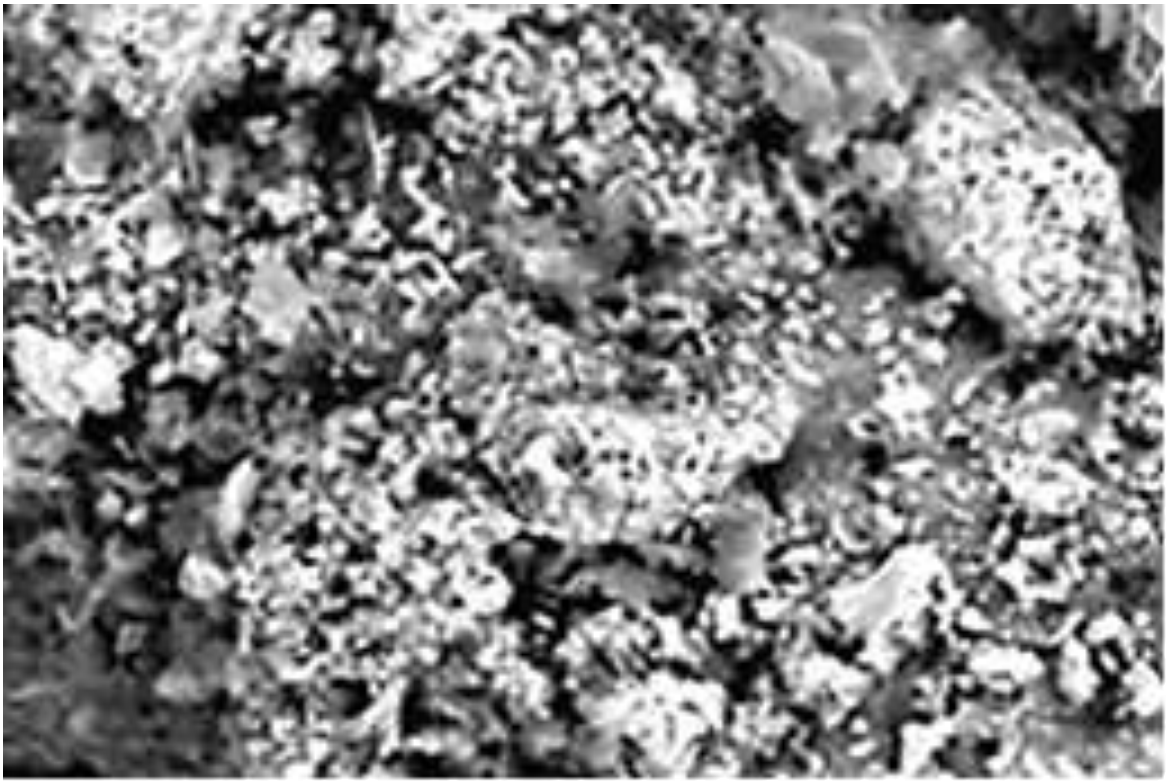

**(b)**

**Fig. 4.** SEM analysis results in ZnO/Fe/Mg/C nanocomposite a **(a)** and ZnO/Fe/Mg/C nanocomposite b **(b)** (SEM images size: 50 nm).

**Table 1.** Energy dispersive spectroscopy of the ZnO/Fe/Mg/C nanocomposite

| **Raman Shifts ($cm^{-1}$)** | **Intensity (counts)** | |
|---|---|---|
| | **ZnO/Fe/Mg/C Nanocomposite a** | **ZnO/Fe/Mg/C Nanocomposite b** |
| 500 | 900 | 625 |
| 1000 | 1450 | 1250 |
| 1500 | 1875 | 1725 |
| 2000 | 1625 | 1375 |
| 2500 | 1975 | 1600 |
| 3000 | 2000 | 1740 |
| 3500 | 2000 | 1740 |
| 4000 | 2000 | 1740 |
| 4500 | 2000 | 1740 |
| 5000 | 2000 | 1740 |

**Table 2.** Elements of ZnO/Fe/Mg/C nanocomposite a, and ZnO/Fe/Mg/C nanocomposite b

| **Elements (wt%)** | **Names of Nanocomposite** | |
|---|---|---|
| | **ZnO/Fe/Mg/C Nanocomposite a** | **ZnO/Fe/Mg/C Nanocomposite b** |
| Zn | 28.39 | 25.00 |
| C | 26.74 | 10.06 |
| Fe | 12.67 | 20.01 |
| Mg | 11.67 | 8.99 |
| O | 13.60 | 4.32 |

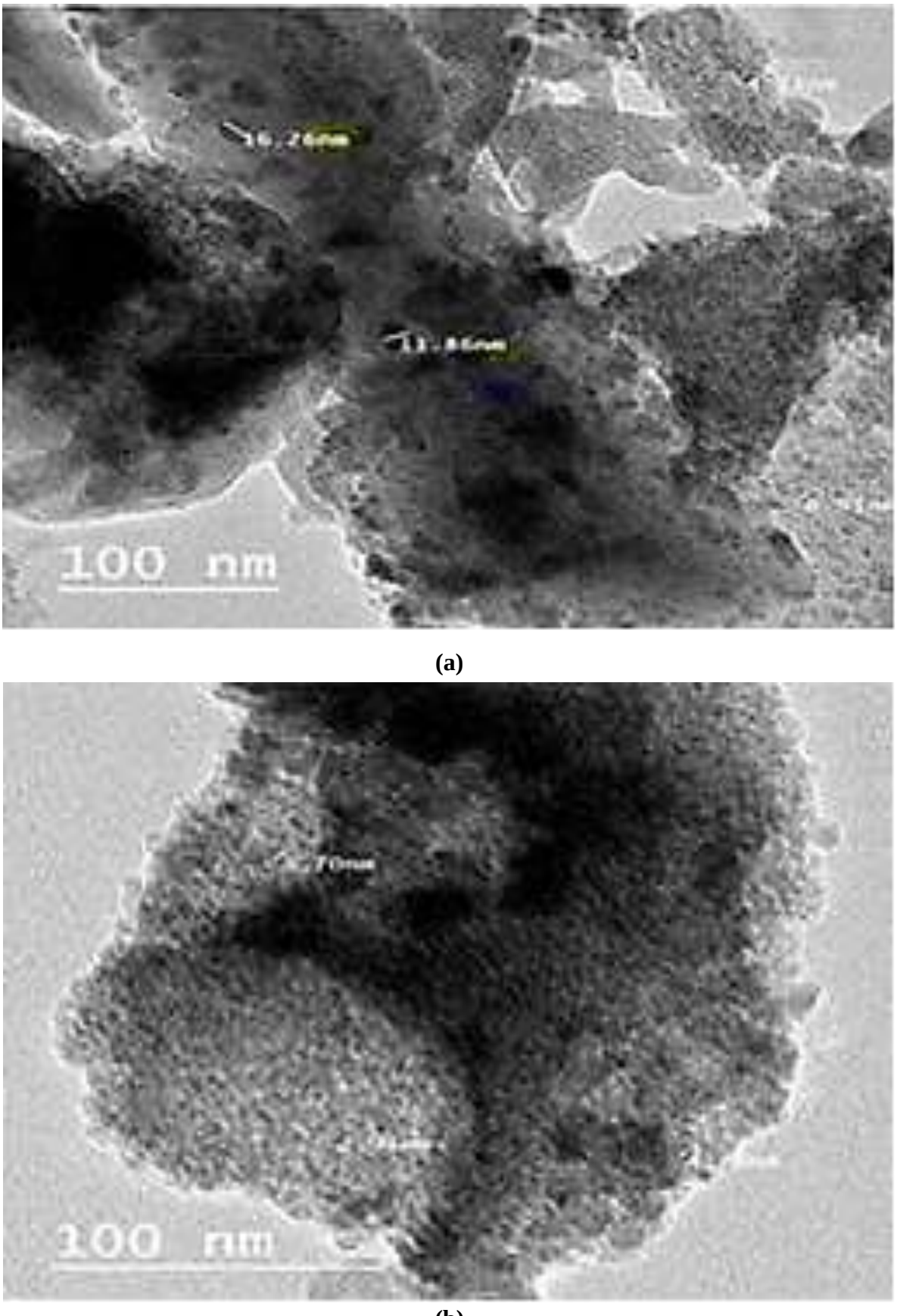


**(a)**

**(b)**

**Fig. 5**. TEM images of the ZnO/Fe/Mg/C nanocomposite a **(a)** and ZnO/Fe/Mg/C nanocomposite b **(b)** (TEM images size: 100 nm).

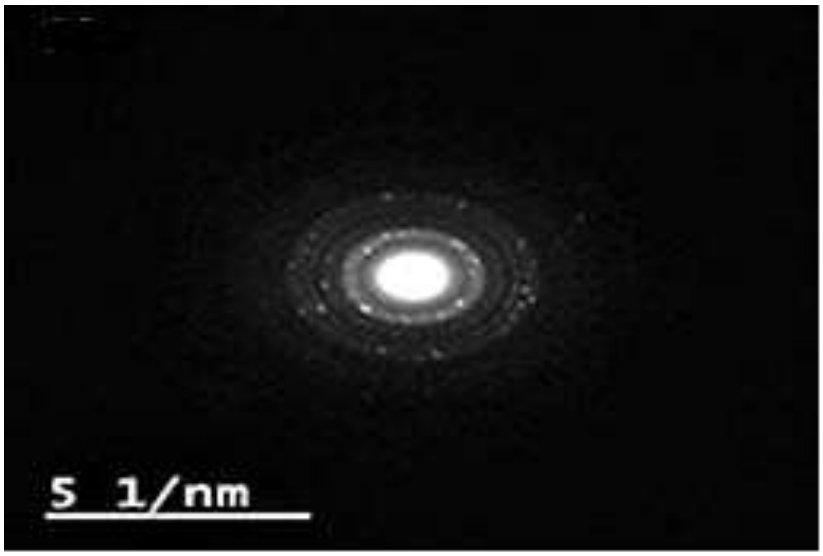


**(a)**

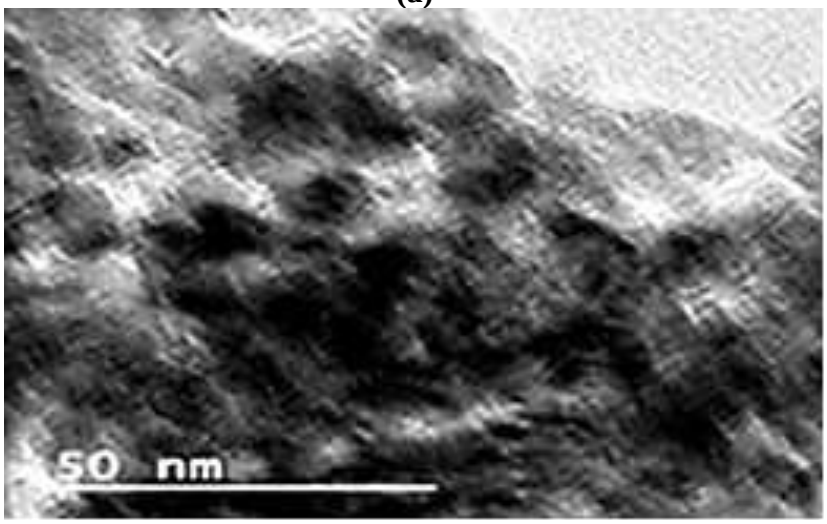


**(b)**

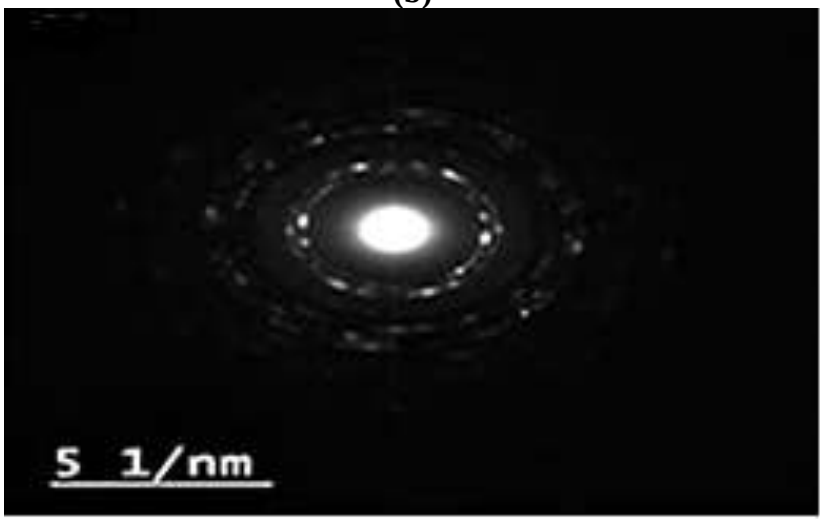


**(c)**

**Fig. 6.** SAED patterns of the ZnO/Mg/C nanocomposite a **(a)**, Fe-doped ZnO/C/Mg b **(b)** and ZnO/Fe/Mg/C **(c)**

**Table 3**. $H_2$ productions from polyester polyurethane, polyethylene via ZnO-Mg-Ni-Fe-C nanocomposite a and ZnO-Mg-Ni-Fe-C nanocomposite b

| **Microplastic Names** | **Name of Nanocomposite and $H_2$ Production (ml/h)** | |
|---|---|---|
| | **ZnO/Fe/Mg/C Nanocomposite a** | **ZnO/Fe/Mg/C nanocomposite b** |
| Polyester polyurethane | 7800 | 5600 |
| Polyethylene | 9800 | 8700 |

**Table 4.** Effect of ZnO/Fe/Mg/C nanocomposite a, concentration on $H_2$ productions in 250 mg/l polyester polyurethane and polyethylene microplastic concentrations

| **Nanocomposite** | **Microplastic Names and Yields** | |
|---|---|---|
| **ZnO/Fe/Mg/C nanocomposite a, Concentration (mg/l)** | **Photodegradation Yield of Polyethylene (%)** | **Photodegradation Yield of Polyester Polyurethane (%)** |
| 1 | 67 | 59 |
| 3 | 99 | 89 |
| 5 | 98 | 88 |
| 7 | 94 | 80 |
| 10 | 89 | 70 |

**Table 5.** Effect of time on $H_2$ productions in the presence of polyester polyurethane and polyethylene microplastics via 3 mg/l ZnO/Fe/Mg/C nanocomposite a

| **Time** | **Microplastic Type and $H_2$ Yield Percentage (%)** | |
|---|---|---|
| | **Polyethylene** | **Polyester Polyurethane** |
| 3 | 92 | 67 |
| 4 | 99 | 77 |
| 5 | 98 | 82 |
| 6 | 98 | 88 |
| 8 | 97 | 88 |
| 10 | 97 | 87 |
| 15 | 97 | 86 |
| 30 | 97 | 85 |

**Table 6.** Effect of temperature increase on $H_2$ production yields of polyethylene and polyester polyurethane

| Temperature (ºC) | $H_2$ Production Yield (%) from Polyethylene | $H_2$ Production Yield (%) from Polyester Polyurethane |
|---|---|---|
| 35 | 97 | 60 |
| 70 | 98 | 70 |
| 90 | 99 | 80 |
| 125 | 99 | 88 |
| 150 | 99 | 88 |
| 175 | 99 | 99 |